

## Four-Wave-Mixing Approach to *In Situ* Detection of Nanoparticles

Alexandros Gerakis,<sup>1,\*</sup> Yao-Wen Yeh,<sup>2</sup> Mikhail N. Shneider,<sup>3</sup> James M. Mitrani,<sup>1</sup>  
Brentley C. Stratton,<sup>1</sup> and Yevgeny Raitses<sup>1</sup>

<sup>1</sup>*Princeton Plasma Physics Laboratory, 100 Stellarator Road, Princeton, New Jersey 08540, USA*

<sup>2</sup>*Princeton Institute for Science and Technology of Materials, Princeton University,  
Princeton, New Jersey 08544, USA*

<sup>3</sup>*Department of Mechanical and Aerospace Engineering, Princeton University,  
Princeton, New Jersey 08540, USA*



(Received 24 August 2017; revised manuscript received 2 December 2017; published 29 January 2018)

We report on the development and experimental validation of a laser-based technique which uses coherent Rayleigh-Brillouin scattering (CRBS) to detect nanoparticles with characteristic sizes ranging from the atomic scale to tens of nanometers. This technique is aimed (nonexclusively) at the detection of nanoparticles produced by volumetric nanoparticle synthesis methods. Using CRBS, carbon nanoparticles of dimensions less than 10 nm and concentrations of  $10^{10} \text{ cm}^{-3}$  are detected *in situ* in a carbon arc discharge with graphite electrodes. This four-wave-mixing approach should enable advances in the understanding of nanoparticle growth that could potentially lead to improved modeling of the growth mechanisms, and thus to improve synthesis selectivity of nanoparticles and yield.

DOI: 10.1103/PhysRevApplied.9.014031

### I. INTRODUCTION

Volumetric nanoparticle synthesis methods, such as flames [1,2], arc discharges [3–5], and laser ablation [6], have shown great potential for the production of industrial-scale quantities of various types of nanoparticles [7,8] with different structures, such as fullerenes [6], carbon [9] and boron nitride nanotubes [7,10], nanowires [11], etc. Optimization of these techniques requires a better understanding and control of the nanoparticle synthesis process to increase nanoparticle selectivity and produce nanostructures with the desired structural characteristics and properties. For typical volumetric synthesis conditions, there are no conventional *in situ* optical diagnostic methods capable of resolving subnanometer- and nanometer-scale nanoparticles.

Because of the harsh environment in which nanoparticle nucleation and growth usually occur (e.g., high temperatures), detection is usually done via optical techniques, which are less perturbing than other techniques such as mechanical extractors [12]. A number of diagnostic tools are employed to map the nanoparticle formation process from the precursor atoms and molecules to the end product. Species identification and measurements of temperatures and relative atomic and molecular densities can be obtained from optical emission spectroscopy, in which collisionally excited light emitted from the nanoparticle synthesis region is spectroscopically resolved [13,14]. Laser-induced fluorescence provides quantitative measurements of atomic

and molecular densities [15]. The sizes of nanoparticles of dimensions larger than 20 nm can be measured via laser-induced incandescence, in which particles are heated by a laser beam and the decay time of the resulting incandescence is measured and modeled [16]. The intermediate regime between initial nucleation and nanoparticle growth particles with sizes of 10–20 nm is particularly challenging for nanoparticle detection. The only optical technique previously applied in this regime is Raman spectroscopy [17]. However, Raman spectroscopy probes nanoparticle structure only and does not provide nanoparticle dimensional information. Nanoparticles in this regime have been detected using x-ray radiation from synchrotron sources to perform small-angle x-ray scattering [18–20]. Although successful, this technique requires access to a collimated synchrotron light source, which can be costly and infrequent. Thus, nanomaterials research would benefit from a nanoparticle detection technique based on a tabletop laser system. In this paper, we demonstrate the use of coherent Rayleigh-Brillouin scattering (CRBS), a proven laser-based gas measurement technique [21,22], for the *in situ* volumetric detection of nanoparticles in an arc discharge.

### II. COHERENT RAYLEIGH-BRILLOUIN SCATTERING: AN OVERVIEW

CRBS is a nonresonant four-wave-mixing process which relies on inducing an electrostrictive grating through the interference of two intense laser beams, termed the *pump* beams, within a medium. The pump beams have a wavelength of  $\lambda_{\text{pump}}$  and identical polarization (Fig. 1).

\*agerakis@pppl.gov

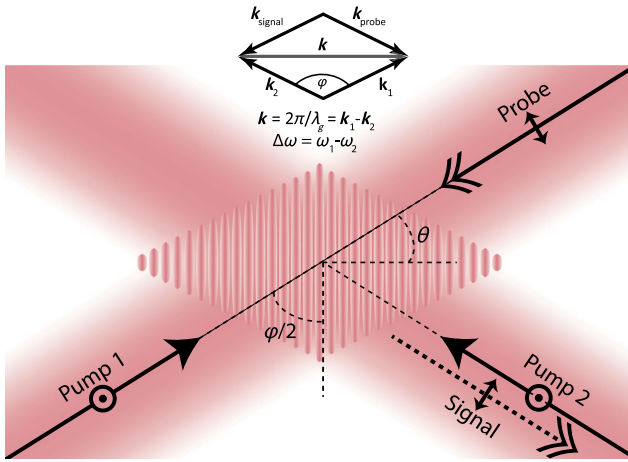


FIG. 1. Typical planar CRBS geometry. Two nearly counter-propagating pump beams of the same polarization interfere within a medium to create an optical lattice. A probe beam with polarization normal to that of the pumps is incident on this lattice at the Bragg angle to give the fourth beam, the signal beam.

By varying the frequency difference  $\Delta f$  of the pump beams, an optical lattice moving at a phase velocity given by  $v_g = (\Delta f \lambda_{\text{pump}}) / [2 \sin(\phi/2)]$  is created. Individual particles that have a translational velocity equal to or close to  $v_g$  feel an attraction toward the high-intensity regions of the interference pattern due to the optical dipole force [23]. Thus, the density modulation induced in the medium effectively probes the velocity distribution function of the medium as  $\Delta f$  is scanned. The wavelength  $\lambda_g$  of the resulting optical lattice is determined by the crossing half angle  $\phi/2$  of the pump beams through the relation  $\lambda_g = \lambda_{\text{pump}} / [2 \sin(\phi/2)]$  (Fig. 1).

A third beam, called the probe, with wavelength  $\lambda_{\text{probe}}$  and polarization normal to that of the pumps, is incident upon the optical lattice at an angle  $\theta$  that fulfills the first-order Bragg condition  $\lambda_{\text{probe}} = \lambda_g \sin(\theta)$  [24]. A fourth beam, termed the *signal*, is generated through the interaction of the probe beam with the optical lattice. A CRBS spectrum is obtained by measuring the intensity of the signal beam versus the optical lattice velocity. The CRBS signal intensity  $I_S$  is proportional to the square of the induced refractive-index modulation,  $I_S \propto L^2 (\Delta n)^2 I_1 I_2 I_{\text{pr}} \propto \Delta n^2$ , where  $I_1$  and  $I_2$  are the pump intensities,  $L$  is the length of the interaction region,  $I_{\text{pr}}$  is the probe intensity and  $\Delta n = [(\alpha_{\text{eff}} \Delta N) / (2\epsilon_0)]$ , where  $\alpha_{\text{eff}}$  is the effective polarizability of the particles (atoms or molecules) and  $\Delta N$  is the induced periodic density modulation [22,25]. In comparison to spontaneous Rayleigh scattering, in which scattering occurs into a  $4\pi$  solid angle, the CRBS signal is a laser beam with the characteristics of the probe beam. CRBS has proven to be a powerful technique for the determination of the temperature, speed of sound, pressure, polarizability, shear, and bulk viscosity of a gas or gas mixture [25–29].

The size of the particles that can be detected by CRBS is determined by the Rayleigh criterion, which defines the maximum particle dimension that can be observed as  $\lambda/10$ , where  $\lambda$  is the detection wavelength. CRBS has never before been applied to gas-nanoparticle mixtures. Nanoparticle detection with CRBS was initially suggested in Ref. [30], which examined the feasibility of detecting  $C_{60}$  in an atmospheric-pressure argon background. The resulting CRBS line shape is dominated by the Rayleigh peak since phonons cannot be launched in nanoparticle ensembles at such low densities. This detection technique preferentially measures the smallest nanoparticles in the measurement region since the Rayleigh peaks of heavier particles would be masked by the Rayleigh peaks of lighter particles. For an ensemble of nanoparticles with known or estimated temperature, the mass of the detected nanoparticles can be derived from the width of the Rayleigh peak. By calibrating the CRBS signal intensities in known conditions (e.g., atmospheric-pressure air), reliable estimates of the nanoparticle densities can also be obtained from the Rayleigh peak amplitude [25].

### III. CRBS EXPERIMENTAL SETUP

CRBS has been applied to the *in situ* detection of carbon nanoparticles produced by an arc discharge. The dc arc operates in the reactor chamber between two 6-mm-diameter graphite electrodes with an interelectrode gap of approximately 4 mm in a helium atmosphere of 500 Torr. This setup is similar to the one used for the initial demonstration of the production of carbon fullerenes [31] and nanotubes [32]. The arc current ranges from 40 to 60 A; the arc voltage is maintained at about 25 V. The graphite anode ablates during arc operation, and evaporated carbon products deposit on the cathode and chamber walls [4].

The CRBS system used in this work is described in detail elsewhere [25,33]. The two pump laser beams and the probe beam have a wavelength of  $\lambda_{\text{pump}} = \lambda_{\text{probe}} = 1064$  nm and a pulse duration of approximately 150 ns, and they can achieve energies of up to about 250 mJ/pulse per beam. The system utilizes the single-shot chirped lattice approach to obtain the CRBS spectrum, with chirp rates as high as  $\Delta f = 1.5$  GHz over the pulse duration [34]. In this approach, all of the velocity components required to obtain a CRBS spectrum are present during a single laser pulse. This approach is important since nanoparticles are expected to have a residence time of approximately 1 ms [35] in the CRBS interaction region, which typically has a spatial extent of about 150  $\mu\text{m}$ . The arc typically operates for approximately 2 min (limited by vacuum-chamber heating). Thus, fast spectral acquisition times are required, which nonchirped CRBS configurations, with acquisition times on the order of 5–10 min, cannot achieve. The CRBS beams cross at a distance of about 13 mm from the arc core where nanoparticles are expected to form (Fig. 2) [12,35]. Helium is not expected to contribute to the

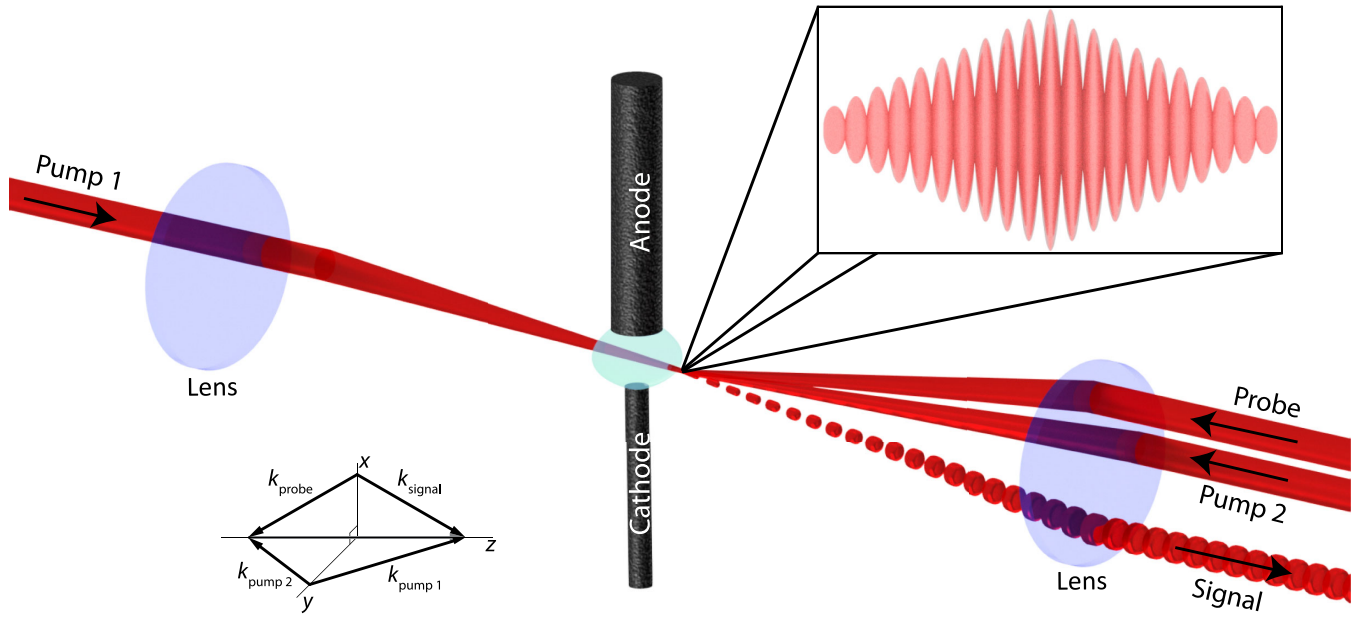


FIG. 2. The folded CRBS geometry used in the experiment described in this paper. Two counterpropagating, coplanar, and equipolarized pump beams are focused by two  $f = 500$  mm lenses to interfere at a distance of 13 mm from the arc core, formed between two graphite electrodes when a current of 50–60 A runs through them. For a CRBS signal beam to be produced, a probe beam, with its polarization normal to that of the pumps, must be incident on the induced optical lattice at the Bragg angle. In order for the background noise from the pumps to be minimized in the line of sight of the resulting CRBS signal beam, the probe is incident on the optical lattice from the plane perpendicular to that of the pumps. It is also important for the interaction region to be formed on the side from which the probe enters so that the signal does not pass through the arc core and weaken due to scattering and absorption.

CRBS signal due to its very small polarizability [25]. The typical planar CRBS geometry (Fig. 1) is not optimal for nanoparticle detection in an arc discharge because the pump beam counterpropagating the signal beam is Rayleigh and Mie scattered from nanoparticles in its path [21,22,25,27,29,34]. The pump beam is also scattered and depolarized, contributing a large background signal to the measurements. To overcome this unwanted background signal, a folded geometry with the probe incident on the lattice from a plane normal to the plane of propagation of the pumps is used, as shown in Fig. 2. This approach ensures that there is minimal unwanted scattering in the line of sight of the signal beam. Another way to overcome this unwanted background signal would be to use a probe of different wavelength and to use spectral filtering to eliminate unwanted scattering of the pumps.

#### IV. *IN SITU* DETECTION OF NANOPARTICLES WITH CRBS

In gases, a single-shot CRBS spectrum can be obtained using an optical lattice with the zero velocity component in the temporal center of the pulse, with chirping to nonzero velocities toward the beginning and the end of the pulse [25,34]. In the case of carbon nanoparticle measurements, the laser intensities required to obtain a CRBS signal ( $10^{14}$  W m $^{-2}$  per beam) are sufficient to destroy the

nanoparticles since carbon nanoparticles have an absorption maximum close to the wavelength used [36]. For other nanoparticles, such as boron nitride nanoparticles, this effect would be less important since the absorption maximum is in the ultraviolet region. This effect is clearly demonstrated in Fig. 3, which shows the CRBS signal (the red lines) for six different applied optical lattice velocity ranges (the black lines). If the nanoparticles are not destroyed, the resulting CRBS spectrum is reproduced regardless of the temporal location of the zero velocity component during the pulse. In our measurements, only the initial part of the pulse produces a useful CRBS signal since the nanoparticles have been destroyed due to laser evaporation by times later in the pulse. This effect has also been observed in studies in which x rays have been used to probe similar structures [37,38] and is known as *diffraction before destruction*. For CRBS, we refer to this phenomenon as *scattering before destruction*.

Although the folded geometry employed in our experiments minimizes the background signal, some background signal is observed, as seen in Fig. 3. The CRBS signal sits on top of this background, which is due to Rayleigh and Mie scattering of the pumps from nanoparticles in the vicinity of the arc. Since there is no useful information in the signal at the end of the pulse, we measure the ratio of the signal in the initial part of the pulse, which is the time interval before the nanoparticles are destroyed and

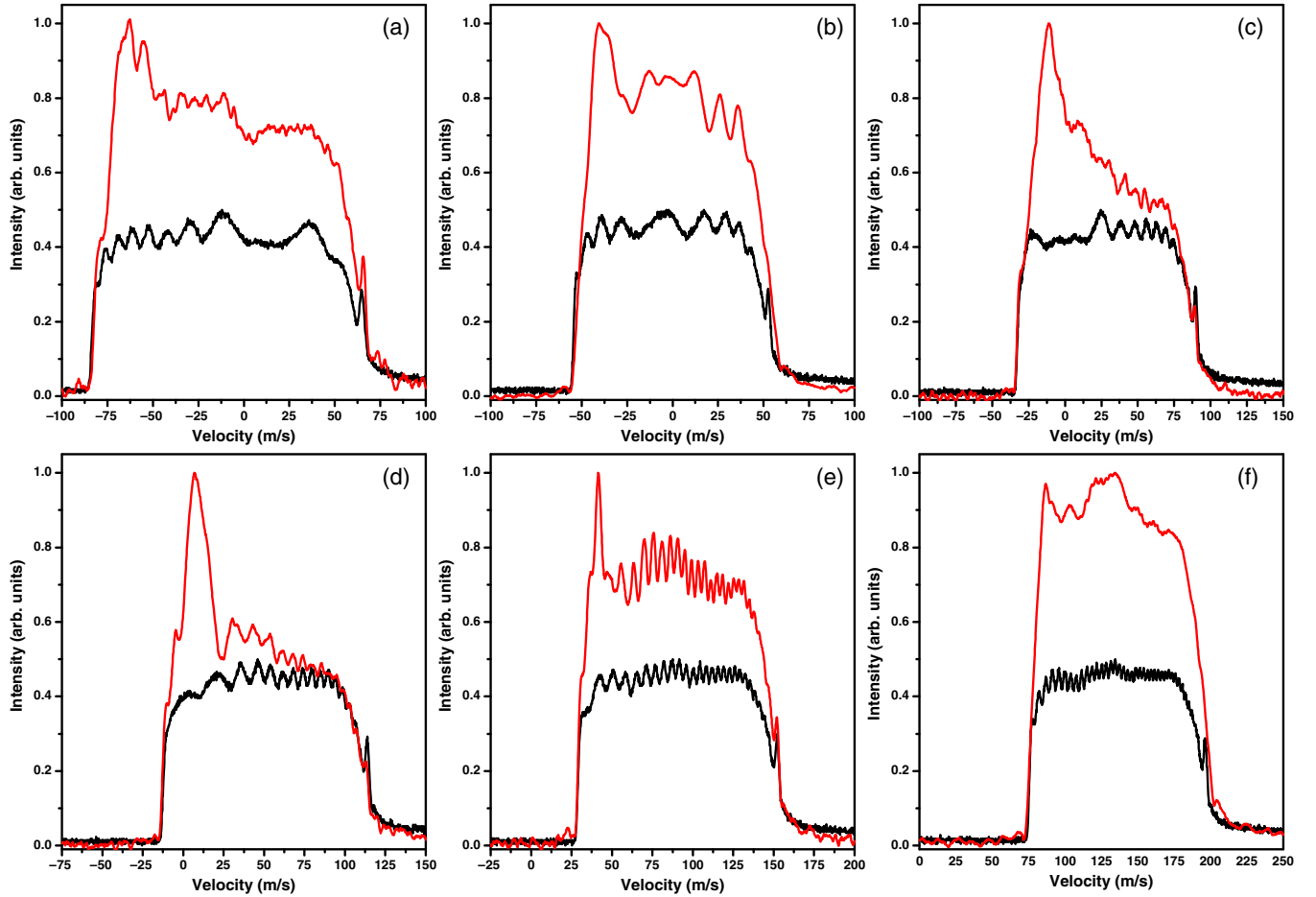


FIG. 3. CRBS signals from the arc (the red lines) for different chirp rates (a), (b), (c), (d), (e), (f), recorded by beating the two pump beams on a fast photodiode (the black lines).

constitutes the scattering-before-destruction CRBS signal, to the signal in the final part of the pulse, which is simply the background level. This measurement is done for a series of scanned velocity ranges, such as those shown in Fig. 3, to reconstruct the nanoparticle Rayleigh peak profile. This approach assumes a uniform particle size distribution and a uniform density per shot for the 10-Hz laser-pulse repetition rate.

The ratio of the CRBS signal to the background signal plotted versus the lattice phase velocity at the beginning of the laser pulse is shown in Fig. 4 (the black dots). This plot represents the CRBS spectrum, which has a maximum value at zero lattice phase velocity. The measured data points are fitted to reconstruct the Rayleigh peak, given the assumptions mentioned earlier (the dashed line). For an estimated temperature  $T$  of 1500 K at the measurement location [16,35], the mass  $m$  of the nanoparticles is calculated from  $e^{-(mv^2/2kT)}$ , where  $v$  is the velocity and  $k$  is Boltzmann's constant (the red line). From this fit, the nanoparticle mass is estimated to be about 500 000 atomic mass units (amu). For comparison, the Rayleigh peak is also calculated for  $C_{60}$ , which has a mass of 720 amu and a

diameter of 7 Å (the orange line). Assuming that the density of the nanoparticles is the same as for  $C_{60}$  (1.72 g/cm<sup>3</sup>) and have a mass that is approximately 700 times larger, then the measured nanoparticles have dimensions of about 6 nm. This result assumes the presence of hollow nanoparticles, such as nanotubes or fullerenes. If a density equal to that of solid graphite (e.g., soot) is assumed (2.266 g/cm<sup>3</sup>), the particles each have a dimension of approximately 5 nm.

It is important to note that this result represents a lower size detection limit since heavier, larger particles could also contribute to the observed CRBS signal. Since their Rayleigh peak width is smaller, their presence is masked by the Rayleigh peak of the lighter particles. It is also important to note that, since the laser fluences used are about 10<sup>14</sup> W m<sup>-2</sup>, scattering before destruction would only give a CRBS signal for the initial size of the nanoparticles, as these nanoparticles would immediately be broken down into their constituents and not just modified to smaller-sized particles. This effect is also suggested by the simulation presented in Fig. 5. Also, if size modification or alteration would indeed take place, this would be

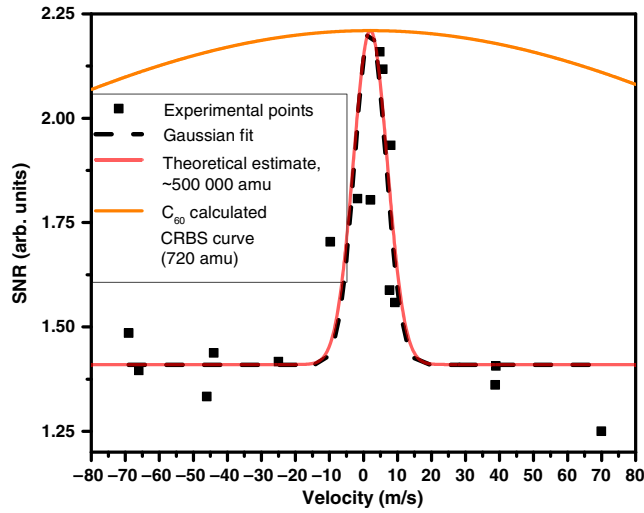


FIG. 4. Reconstructed Rayleigh profile for nanoparticles measured approximately 1.3 cm from the arc core (the red line). This estimate is derived from the ratio of the scattering-before-destruction CRBS signal at the beginning of the laser pulse to the background level (the black dots). Each dot represents the ratio for the CRBS signal over a single laser shot. Also plotted for comparison is the simulated profile for  $C_{60}$  (the orange line).

manifested with a much wider Rayleigh peak, which is only mass dependent for a given temperature.

This result is consistent within an order of magnitude with measurements performed in similar conditions with other methods [12,16]. This result assumes the detection of spherical particles. In order for particle elongation or asymmetry to be detected, one would need to monitor the scattered polarization ratio since spherical particles would scatter the same polarization as that of the probe, while elongated particles would scatter only the polarization projection to their elongated axis. Although elongated nanoparticles, such as nanotubes, are randomly oriented in volumetric synthesis environments, through polarization monitoring we should also be able to identify any potential alignment of these nanoparticles to external fields. This is something we plan to do in the future. Additionally, since clustering is a time-dependent dynamic process or a process occurring in a stream in different spatial areas, then, by observing the change in the shape of the CRBS signal, it would also be possible to detect nanoparticle clustering, in combination with the aforementioned simultaneous polarization monitoring. The peak signal level corresponds to that from air at a pressure of 30 Torr, which yields a measured nanoparticle density of about  $10^{10}$   $\text{cm}^{-3}$  using our detection system calibration [25]. It has to be pointed out that CRBS in the counterpropagating geometry used here has a theoretical detection limit of  $10^8$   $\text{cm}^{-3}$ , which arises from the necessity of having at least one occupant per lattice site in order to obtain a coherent signal. Finally, a strong correlation between the observable CRBS signal and the arc current is observed: as the arc current decreases, the

CRBS signal also decreases, while as the arc current increases, the CRBS signal increases. The same effect is also observed as the measurement location changes: closer to the arc center, the CRBS signal disappears, as there is no nanoparticle production there.

## V. SCATTERING BEFORE DESTRUCTION: THEORETICAL ESTIMATES

To understand the effect of high laser intensities on spherical graphitic nanoparticles, we numerically calculate the time-resolved nanoparticle diameter profiles during and after the laser pulses by solving three coupled ordinary differential equations for the nanoparticles energy, charge, and mass balance. The appropriate energy balance equation is

$$\dot{U}_{\text{int}} = Q_{\text{arc}} + Q_{\text{las}} - Q_{\text{sub}} - Q_{\text{con}} - Q_{\text{rad}} - Q_{\text{the}}, \quad (1)$$

where  $\dot{U}_{\text{int}}$  is the rate of change of the nanoparticle internal energy [39], and the terms denoted by  $Q$  describe the following heat-transfer processes: (1)  $Q_{\text{arc}}$  describes radiative heating from the arc-discharge plasma channel [40], (2)  $Q_{\text{las}}$  describes absorption of energy from the laser pulse using the Rayleigh approximation [41,42] (assuming a complex index of refraction of  $1.57 - 0.56i$  [43]), (3)  $Q_{\text{sub}}$  describes thermal conduction from the evaporative cooling due to laser-induced sublimation [44,45], (4)  $Q_{\text{con}}$  describes thermal conduction from the nanoparticle surface to the ambient gas in the free-molecular-flow regime [39]), (5)  $Q_{\text{rad}}$  describes thermal radiation, and (6)  $Q_{\text{the}}$  describes thermionic emission from laser-heated nanoparticles [40,46]. The charge-balance equation considers a volumetric buildup of positive charge in the nanoparticle due to the thermionic emission of electrons [46]. The mass balance equation considers mass loss from laser-induced sublimation; for spherical nanoparticles, nanoparticle diameter is related to mass by  $\rho_S[(\pi D^3)/6]$ , where  $\rho_S \sim 2$   $\text{g}/\text{cm}^3$  is the density of graphite and  $D$  is the nanoparticle diameter. The formula used for modeling nanoparticle mass loss is

$$\frac{dM}{dt} = -\pi D(t)^2 \frac{W[T(t)]p_V[T(t)]}{R_p T(t)} \sqrt{\frac{R_M T(t)}{2\pi W[T(t)]}}, \quad (2)$$

where  $T(t)$  is the nanoparticle's time-resolved temperature profile,  $R_M$  is the ideal gas constant in effective mass units ( $8.3145 \times 10^7$   $\text{g cm}^2/\text{mol K s}^2$ ),  $R_p$  is the ideal gas constant in effective pressure units ( $83.145$   $\text{bar cm}^3/\text{mol K}$ ), and  $W[T(t)]$  and  $p_V[T(t)]$  are the mean temperature-dependent values of the molecular weight and vapor pressure of the sublimed carbon clusters, respectively. The formulas used for  $W[T(t)]$  and  $p_V[T(t)]$  [44] are calculated from the fits to data published in Leider *et al.* [45].

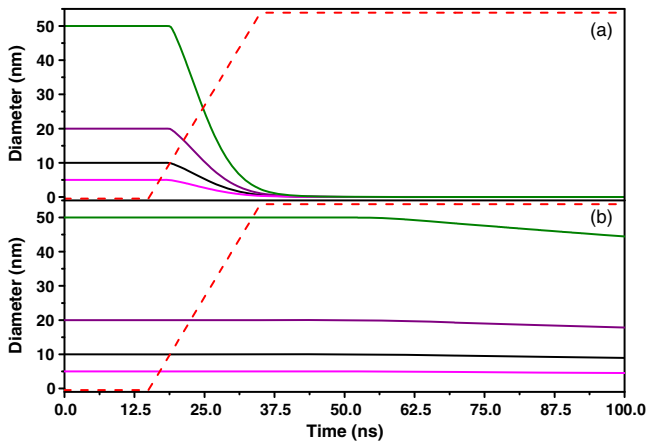


FIG. 5. Simulations of time-resolved nanoparticle diameter profiles (the solid lines) following interaction with a laser pulse (the dashed line) of (a)  $10^{12} \text{ W m}^{-2}$  and (b)  $10^{10} \text{ W m}^{-2}$ .

Numerically solving the energy, charge, and mass balance equations yields the time evolutions of the nanoparticle diameters shown in Fig. 5, which illustrate the trend of increased nanoparticle evaporation with increased laser intensity. The data presented in Fig. 5, which are derived from Eqs. (1) and (2), are meant to qualitatively show that higher laser intensities will destroy carbon nanoparticles with diameters ranging from 5 to 50 nm. There are certainly uncertainties in the terms used in Eqs. (1) and (2), but using any reasonable parameters, from, e.g., Ref. [44], would produce a similar result: laser intensities in excess of  $10^{13} \text{ W m}^{-2}$  are high enough to completely and almost instantaneously destroy carbon nanoparticles.

Figure 5(b) shows that laser-induced sublimation would result in about a 10%–30% reduction in nanoparticle diameters for nanoparticles with different initial diameters in the range 5–50 nm, assuming a laser intensity of  $10^{10} \text{ W m}^{-2}$ . However, a higher laser intensity of  $10^{12} \text{ W m}^{-2}$  results in stronger laser-induced nanoparticle sublimation, and the complete destruction of laser-heated nanoparticles, as shown in Fig. 5(a). This simplified calculation illustrates the worst-case scenario. In reality, the laser intensity seen by the nanoparticles can be lower due to scattering and absorption in a process of the passage through a mixture of gas, nanoparticles, and soot particles adjacent to the observation area. In addition, as the nanoparticles evaporate, they become surrounded by a dense, strongly absorbing cloud, which shields them from further absorption of the incident laser energy. This mechanism would considerably slow down complete nanoparticle evaporation due to absorption.

## VI. CONCLUSIONS

In summary, we report in this paper on an *in situ* detection of nanoparticles of 5 to 6 nm, with concentrations of  $10^{10} \text{ cm}^{-3}$  synthesized in a carbon arc. The results

presented here could allow for the *in situ* detection and monitoring of volumetric nanoparticle formation and growth using a tabletop laser system. CRBS could also be applied to the detection of nanoparticles in other gas-phase synthesis methods (e.g., laser, flame, or plasma torch), as long as the density of nanoparticles is above the CRBS detection limit of CRBS for nanoparticles (approximately  $10^8 \text{ cm}^{-3}$ ). For an estimated temperature at the point of measurement of 1500 K, the average mass of the measured nanoparticles is estimated to be 500 000 amu. Thus, for a known shape of the measured nanoparticles (e.g., from *ex situ* evaluation), the average size of nanoparticles can accurately be deduced if the temperature is known from an independent measurement. We plan to do this in the future. We are working on increasing the detection sensitivity of our system to allow nanoparticles to be detected without destroying them. This would also allow us to directly obtain a CRBS spectrum in a single laser shot (as is the case in gases), in comparison to the tens of shots that are required in the current setup.

The digital data in this paper are available online [47].

## ACKNOWLEDGMENTS

The authors would like to acknowledge Dr. Arthur Dogariu, Dr. Biswajit Santra, and Professor Roberto Car of Princeton University, and Dr. Vladimir Semak of Signature Science for the fruitful discussions, as well as Mr. Alexandr Merzevskiy of Princeton Plasma Physics Laboratory for his technical assistance. This work was supported by the U.S. Department of Energy, Office of Science, Basic Energy Sciences, Materials Sciences and Engineering Division.

- 
- [1] H. K. Kammler, L. Mädler, and S. E. Pratsinis, Flame synthesis of nanoparticles, *Chem. Eng. Technol.* **24**, 583 (2001).
  - [2] S. Li, Y. Ren, P. Biswas, and S. D. Tse, Flame aerosol synthesis of nanostructured materials and functional devices: Processing, modeling, and diagnostics, *Prog. Energy Combust. Sci.* **55**, 1 (2016).
  - [3] J. H. J. Scott and S. A. Majetich, Morphology, structure, and growth of nanoparticles produced in a carbon arc, *Phys. Rev. B* **52**, 12564 (1995).
  - [4] Y.-W. Yeh, Y. Raitses, and N. Yao, Structural variations of the cathode deposit in the carbon arc, *Carbon* **105**, 490 (2016).
  - [5] N. G. Chopra, R. J. Luyken, K. Cherrey, V. H. Crespi, M. L. Cohen, S. G. Louie, and A. Zettl, Boron nitride nanotubes, *Science* **269**, 966 (1995).
  - [6] H. W. Kroto, J. R. Heath, S. C. O'Brien, R. F. Curl, and R. E. Smalley,  $C_{60}$ : Buckminsterfullerene, *Nature (London)* **318**, 162 (1985).

- [7] K. S. Kim, C. T. Kingston, A. Hrdina, M. B. Jakubinek, J. Guan, M. Plunkett, and B. Simard, Hydrogen-catalyzed, pilot-scale production of small-diameter boron nitride nanotubes and their macroscopic assemblies, *ACS Nano* **8**, 6211 (2014).
- [8] A. Fathalizadeh, T. Pham, W. Mickelson, and A. Zettl, Scaled Synthesis of Boron Nitride Nanotubes, Nanoribbons, and Nanococoons Using Direct Feedstock Injection into an Extended-Pressure, Inductively-Coupled Thermal Plasma, *Nano Lett.* **14**, 4881 (2014).
- [9] S. Iijima and T. Ichihashi, Single-shell carbon nanotubes of 1-nm diameter, *Nature (London)* **363**, 603 (1993).
- [10] J. Cumings and A. Zettl, Mass-production of boron nitride double-wall nanotubes and nanococoons, *Chem. Phys. Lett.* **316**, 211 (2000).
- [11] K. F. Huo, Z. Hu, F. Chen, J. J. Fu, Y. Chen, B. H. Liu, J. Ding, Z. L. Dong, and T. White, Synthesis of boron nitride nanowires, *Appl. Phys. Lett.* **80**, 3611 (2002).
- [12] X. Fang, A. Shashurin, G. Teel, and M. Keidar, Determining synthesis region of the single wall carbon nanotubes in arc plasma volume, *Carbon* **107**, 273 (2016).
- [13] P. Byszewski, H. Lange, A. Huczko, and J. F. Behnke, Fullerene and nanotube synthesis. Plasma spectroscopy studies, *J. Phys. Chem. Solids* **58**, 1679 (1997).
- [14] A. Seiji, A. Hiroshi, and N. Yoshikazu, Optical emission spectroscopy of arc flame plasma for generation of carbon nanotubes, *Jpn. J. Appl. Phys.* **39**, 4939 (2000).
- [15] M. Cau, N. Dorval, B. Attal-Trétout, J. L. Cochon, A. Foutel-Richard, A. Loiseau, V. Krüger, M. Tsurikov, and C. D. Scott, Formation of carbon nanotubes: *In situ* optical analysis using laser-induced incandescence and laser-induced fluorescence, *Phys. Rev. B* **81**, 165416 (2010).
- [16] S. Yatom, J. Bak, A. Khrabryi, and Y. Raitses, Detection of nanoparticles in carbon arc discharge with laser-induced incandescence, *Carbon* **117**, 154 (2017).
- [17] X. Liu, M. E. Smith, and S. D. Tse, *In situ* Raman characterization of nanoparticle aerosols during flame synthesis, *Appl. Phys. B* **100**, 643 (2010).
- [18] G. Beaucage, H. K. Kammler, R. Mueller, R. Strobel, N. Agashe, S. E. Pratsinis, and T. Narayanan, Probing the dynamics of nanoparticle growth in a flame using synchrotron radiation, *Nat. Mater.* **3**, 370 (2004).
- [19] J. B. A. Mitchell, J. L. LeGarrec, M. Sztucki, T. Narayanan, V. Dikhtyar, and E. Jerby, Evidence for Nanoparticles in Microwave-Generated Fireballs Observed by Synchrotron X-Ray Scattering, *Phys. Rev. Lett.* **100**, 065001 (2008).
- [20] F. Ossler, S. E. Canton, and J. Larsson, X-ray scattering studies of the generation of carbon nanoparticles in flames and their transition from gas phase to condensed phase, *Carbon* **47**, 3498 (2009).
- [21] J. H. Grinstead and P. F. Barker, Coherent Rayleigh Scattering, *Phys. Rev. Lett.* **85**, 1222 (2000).
- [22] X. Pan, M. N. Shneider, and R. B. Miles, Coherent Rayleigh-Brillouin Scattering, *Phys. Rev. Lett.* **89**, 183001 (2002).
- [23] R. W. Boyd, in *Handbook of Laser Technology and Applications (Three-Volume Set)* (Taylor & Francis, London, 2003), p. 161.
- [24] W. H. Bragg and W. L. Bragg, The reflection of x-rays by crystals, *Proc. R. Soc. A* **88**, 428 (1913).
- [25] A. Gerakis, M. N. Shneider, and B. C. Stratton, Remote-sensing gas measurements with coherent Rayleigh-Brillouin scattering, *Appl. Phys. Lett.* **109**, 031112 (2016).
- [26] X. Pan, M. N. Shneider, and R. B. Miles, Coherent Rayleigh-Brillouin scattering in molecular gases, *Phys. Rev. A* **69**, 033814 (2004).
- [27] J. Graul and T. Lilly, Coherent Rayleigh-Brillouin scattering measurement of atmospheric atomic and molecular gas temperature, *Opt. Express* **22**, 20117 (2014).
- [28] M. O. Vieitez, E. J. van Duijn, W. Ubachs, B. Witschas, A. Meijer, A. S. de Wijn, N. J. Dam, and W. van de Water, Coherent and spontaneous Rayleigh-Brillouin scattering in atomic and molecular gases and gas mixtures, *Phys. Rev. A* **82**, 043836 (2010).
- [29] A. S. Meijer, A. S. de Wijn, M. F. E. Peters, N. J. Dam, and W. van de Water, Coherent Rayleigh-Brillouin scattering measurements of bulk viscosity of polar and nonpolar gases, and kinetic theory, *J. Chem. Phys.* **133**, 164315 (2010).
- [30] M. N. Shneider and S. F. Gimelshein, Application of coherent Rayleigh-Brillouin scattering for *in situ* nanoparticle and large molecule detection, *Appl. Phys. Lett.* **102**, 173109 (2013).
- [31] S. Iijima, The 60-carbon cluster has been revealed, *J. Phys. Chem.* **91**, 3466 (1987).
- [32] S. Iijima, Helical microtubules of graphitic carbon, *Nature (London)* **354**, 56 (1991).
- [33] A. Gerakis, M. N. Shneider, B. C. Stratton, and Y. Raitses, An all-optical, *in situ* diagnostic for large molecule and nanoparticle detection, *Proc. SPIE Int. Soc. Opt. Eng.* **10093**, 100930O (2017).
- [34] A. Gerakis, M. N. Shneider, and P. F. Barker, Single-shot coherent Rayleigh-Brillouin scattering using a chirped optical lattice, *Opt. Lett.* **38**, 4449 (2013).
- [35] M. Kundrapu and M. Keidar, Numerical simulation of carbon arc discharge for nanoparticle synthesis, *Phys. Plasmas* **19**, 073510 (2012).
- [36] B. Santra, M. N. Shneider, and R. Car, *In situ* characterization of nanoparticles using Rayleigh scattering, *Sci. Rep.* **7**, 40230 (2017).
- [37] H. N. Chapman, C. Coleman, and N. Timneanu, Diffraction before destruction, *Phil. Trans. R. Soc. B* **369**, 20130313 (2014).
- [38] R. Xu, H. Jiang, C. Song, J. A. Rodriguez, Z. Huang, C.-C. Chen, D. Nam, J. Park, M. Gallagher-Jones, S. Kim *et al.*, Single-shot three-dimensional structure determination of nanocrystals with femtosecond x-ray free-electron laser pulses, *Nat. Commun.* **5**, 4061 (2014).
- [39] H. A. Michelsen, P. O. Witze, D. Kayes, and S. Hochgreb, Time-resolved laser-induced incandescence of soot: The influence of experimental factors and microphysical mechanisms, *Appl. Opt.* **42**, 5577 (2003).
- [40] M. N. Shneider, Carbon nanoparticles in the radiation field of the stationary arc discharge, *Phys. Plasmas* **22**, 073303 (2015).
- [41] F. Liu, M. Yang, F. A. Hill, D. R. Snelling, and G. J. Smallwood, Influence of polydisperse distributions of both primary particle and aggregate size on soot temperature in low-fluence LII, *Appl. Phys. B* **83**, 383 (2006).

- [42] C. F. Bohren and D. R. Huffman, *Absorption and Scattering of Light by Small Particles* (John Wiley & Sons, New York, 2008).
- [43] K. C. Smyth and C. R. Shaddix, The elusive history of  $\tilde{m} = 1.57 - 0.56i$  for the refractive index of soot, *Combust. Flame* **107**, 314 (1996).
- [44] H. A. Michelsen *et al.*, Modeling laser-induced incandescence of soot: A summary and comparison of LII models, *Appl. Phys. B* **87**, 503 (2007).
- [45] H. R. Leider, O. H. Krikorian, and D. A. Young, Thermodynamic properties of carbon up to the critical point, *Carbon* **11**, 555 (1973).
- [46] J. M. Mitrani, M. N. Shneider, B. C. Stratton, and Y. Raitses, Modeling thermionic emission from laser-heated nanoparticles, *Appl. Phys. Lett.* **108**, 054101 (2016).
- [47] Dataset available at <http://arks.princeton.edu/ark:/88435/dsp01x920g025r>.